Highly Efficient Asymmetric Power Division and System-Level Integration for Millimeter-Wave SWIPT: Theory, Design, and Experiment

Jiupei Shi, Chaoyun Song, *Senior Member, IEEE*, Yejun He, *Senior Member, IEEE*,
Qiang Hua, *Member, IEEE*, Bo Liu, *Senior Member, IEEE*, Junjie Zheng, *Graduate Student Member, IEEE*,
Jinyao Zhang, Sai-Wai Wong, *Senior Member, IEEE*, and Yi Huang, *Fellow, IEEE*

***Abstract*—Traditionally, simultaneous wireless information and power transfer (SWIPT) has employed equal power division between the communication and rectification paths. However, this symmetric approach is suboptimal, as the power requirements for information decoding and energy harvesting (EH) are inherently different, leading to energy inefficiencies. To overcome this limitation, we propose and experimentally validate an asymmetric power divider (PD) and system-integrated design for millimeter-wave (mmWave) SWIPT. The proposed system integrates an asymmetrically allocated PD, a 4 × 4 circularly polarized (CP) receiving antenna array with a 36.1% impedance bandwidth, a 30.2% axial ratio bandwidth (ARBW), and a 19.6-dBic peak gain, together with a wideband, high-efficiency rectifier circuit. The measurement results demonstrate that the signal-to-noise ratio (SNR) of both the 28-GHz modulated signal and continuous wave (CW) signal at the communication port exceeds 56 dB. At the rectifier port, a maximum RF-to-dc conversion efficiency of 60.5% is achieved when the input power is 18 dBm. This work presents the first system-level experimental verification of an SWIPT system with asymmetric power division operating in the mmWave band. The proposed design offers several advantages, including an adjustable power ratio, broad bandwidth, high gain, high RF-to-dc conversion efficiency, and ease of integration. Therefore, it holds significant potential for future mmWave Internet of Things (IoT) applications and wireless energy, communication, and sensing networks.**

***Index Terms*—Circularly polarized (CP), millimeter-wave (mmWave) power transfer, rectennas, wideband, wireless power transfer (WPT).**

I. INTRODUCTION

WITH the rapid development of implantable medical devices, Internet of Things (IoT) sensors, remote environmental monitoring devices, and so on, there is an increasing need for wireless battery devices. This is mainly due to the strong desire to reduce the frequency of battery replacement, minimize the maintenance cost, and enhance the flexibility of the devices. As a result, wireless power transfer (WPT) and energy harvesting (EH) technologies have emerged as key areas of research focus. They are capable of receiving/capturing RF energy from the natural environment and converting it into direct current (dc) to provide a continuous and stable energy supply for remote wireless devices [1], [2], [3]. The combination of WPT technology and wireless communication technology has resulted in simultaneous wireless information and power transfer (SWIPT) [4], [5], [6], [7]. SWIPT not only realizes the fast and reliable transmission of data but also provides the necessary power for the devices at the receiving end within the same frequency band. It greatly enhances the overall efficiency and utility of the wireless communication system. SWIPT can be implemented using three main architectures: time separated (TS), antenna separated (AS), and power separated (PS) [8], [9], [10], [11]. The TS architecture operates in two distinct phases, one for EH and the other for information demodulation. However, it suffers from inefficiency and increased latency, as EH and data transmission occur sequentially. For the AS architecture, energy and information signals are received via separate antennas. While this allows for simultaneous operation, it incurs disadvantages such as larger device size, higher cost, and more complex installation, making it unsuitable for compact or miniaturized systems. In contrast, the PS architecture splits the received signal into two streams: one for EH and the other for information demodulation. This approach enables true simultaneous transmission and reception, offering lower latency, better resource utilization, and improved suitability for applications with stringent real-time requirements. Consequently, the PS SWIPT architecture is considered the most practical among

Received 22 October 2025; accepted 22 November 2025. This work was supported in part by the National Key Research and Development Program of China under Grant 2023YFE0107900, in part by the National Natural Science Foundation of China (NSFC) under Grant U2541208, in part by the Key Program of Shenzhen Natural Science Foundation under Grant JCYJ20241202124219023, and in part by the Program of Shenzhen Key Laboratory Evaluation under Grant SYSPG20241211173908022. *(Corresponding authors: Chaoyun Song; Yejun He.)*

Jiupei Shi, Chaoyun Song, Yejun He, Junjie Zheng, Jinyao Zhang, and Sai-Wai Wong are with the State Key Laboratory of Radio Frequency Heterogeneous Integration, Sino-British Antennas and Propagation Joint Laboratory of Ministry of Science and Technology of China, Guangdong Engineering Research Center of Base Station Antennas and Propagation, Shenzhen Key Laboratory of Antennas and Propagation, College of Electronics and Information Engineering, Shenzhen University, Shenzhen 518060, China (e-mail: jiupei_shi@163.com; chaoyun.song@kcl.ac.uk; heyejun@126.com; xx566593834@163.com; jyzhang@szu.edu.cn; wongsaiwai@ieee.org).

Qiang Hua is with the Department of Engineering and Technology, School of Computing and Engineering, University of Huddersfield, HD1 3DH Huddersfield, U.K. (e-mail: Q.Hua@hud.ac.uk).

Bo Liu is with the James Watt School of Engineering, University of Glasgow, G12 8QQ Glasgow, U.K. (e-mail: Bo.Liu@glasgow.ac.U.K).

Yi Huang is with the Department of Electrical Engineering and Electronics, University of Liverpool, L69 3BX Liverpool, U.K. (e-mail: huangyi@liverpool.ac.uk).

Digital Object Identifier 10.1109/TMTT.2025.3639282

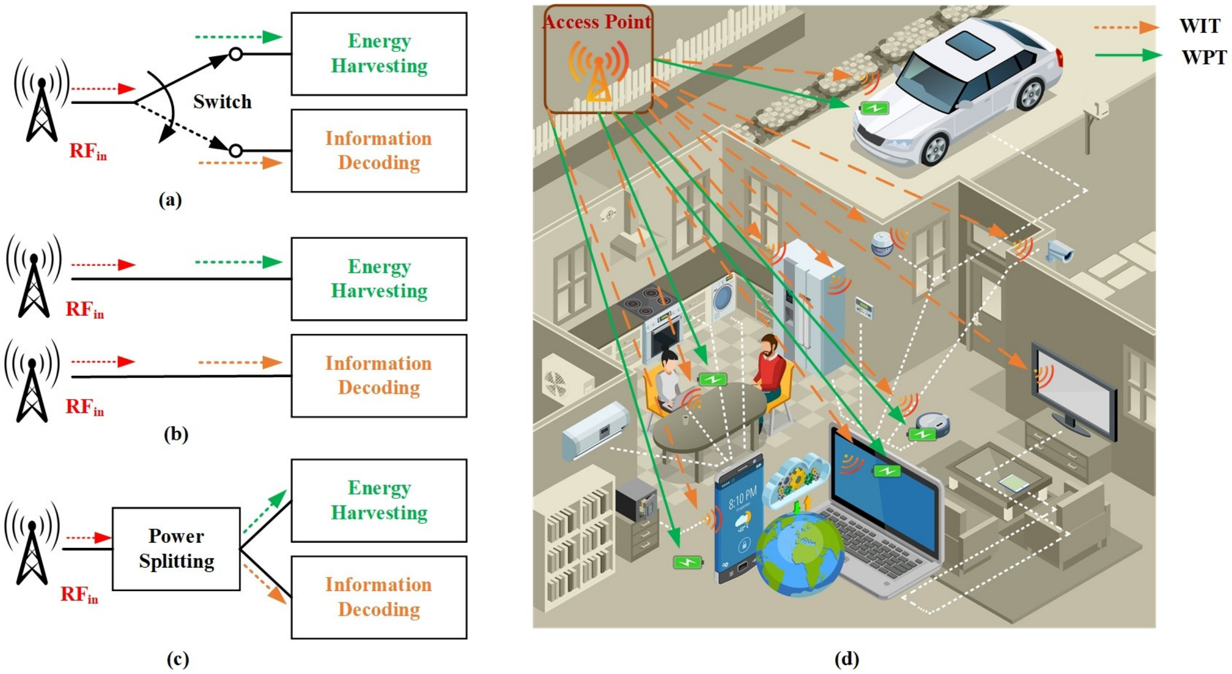

Fig. 1. Three architectures and application scenarios of SWIPT. (a) Time-separated. (b) Antenna-separated. (c) Power-separated. (d) Application scenarios of SWIPT.

them. An overview of three SWIPT architectures and their application scenarios is illustrated in Fig. 1.

Several rectennas have been proposed in the sub-6-GHz band, including single-port [12], [13], [14] and dual-port antennas [15], [16], [17]. Single-port antennas are typically connected to either communication modules or rectifying circuits, allowing them to receive power and data alternately. However, they are incapable of supporting simultaneous data and energy transmission. Dual-port antennas enable concurrent transmission of information and power, but most reported designs suffer from limitations such as operation in separate frequency bands, low RF-to-dc conversion efficiency [15], and poor port isolation [17]. To address frequency calibration in SWIPT systems, some designs utilize antenna elements or arrays connected to an equal power divider (PD), which distributes the received power equally between the rectifying circuit and the communication module [15], [16]. In practice, wireless information (WI) and WPT have different power requirements, with WI typically demanding far less power than WPT [18]. Therefore, to improve the overall efficiency of power utilization, a nonequal PD can be employed to allocate a greater proportion of power to the EH module, enhancing RF-to-dc conversion performance.

The millimeter-wave (mmWave) band (30–300 GHz) plays a vital role in the development of future 5G and beyond wireless networks, as it helps alleviate congestion in the already crowded sub-6-GHz spectrum [19]. Although mmWave signals are highly susceptible to atmospheric attenuation, water absorption, and significant propagation losses, these challenges can be mitigated by leveraging the high directionality of large antenna arrays. Such arrays enhance transmission efficiency and minimize signal scattering losses, making mmWave communication more viable for high-capacity and short-range applications [20], [21], [22], [23]. The short wavelength of mmWave signals enables the design of compact antennas and circuits, which further broadens the potential applications of SWIPT in areas such as IoT and implantable medical devices. The mmWave technology offers opportunities for high data rates and strong directivity. However, achieving reliable and efficient SWIPT at these frequencies is significantly more challenging than at microwave bands. This is due to factors such as higher path loss, susceptibility to blockage, the implementation complexity of rectifiers and highly directional antennas, and the difficulty of integrated device design at mmWave frequencies. Therefore, current research on SWIPT has predominantly focused on the sub-6-GHz band, while studies involving the mmWave band have largely concentrated on WPT, with limited exploration of simultaneous information and power transmission [24], [25], [26], [27], [28], [29] and EH [30], [31], [32], [33], whereas SWIPT research in the mmWave band has not been reported yet. Song et al. [24] designed a new wideband wide-beam mmWave rectenna by using magnetoelectric (ME) dipoles and high-frequency diodes and constructed a multinode charge tracking system based on a leaky wave antenna (LWA). The RF-to-dc conversion efficiency is up to 67% at input power over 15 dBm. A dual-band dual-polarized circularly polarized (CP) receiver antenna is designed in [26]. By loading a curved parasitic patch near a single circular patch to form a chiral structure, integrating two L-node impedance converters and three sector low-pass filters to form a dual-band rectifying circuit, and the two are integrated to form a rectenna. The maximum conversion efficiencies at 24 and 28 GHz are 49.1% and 47.8%, respectively, when the input power is 18 dBm. To enable EH in the mmWave band, a broadband mmWave antenna fabricated on a flexible textile substrate is presented in [31]. The antenna is impedance-matched to the rectifier via a tapered feed line and achieves an RF-to-dc conversion efficiency of 12% at an input power of 10 dBm. A modified Luneburg lens, a dual-polarized ME dipole rectenna, and a simple dc combiner were designed to enhance mmWave EH by leveraging frequency, spatial, and polarization diversity. This system achieved a measured average RF-to-dc conversion efficiency of 60% at an input power of 10 dBm [32].

The use of CP antennas in the design further mitigates multipath fading and reduces polarization mismatch, improving the overall robustness and efficiency of the EH system. For WPT and EH, the relative positions and orientations of the transmitter and receiver may change, and CP antennas can effectively avoid energy loss due to polarization mismatch and improve the robustness of the system [26], [34], [35], [36], [37], [38]. The CP radiation performance is enhanced through the innovative introduction of the complementary source technique in [34]. This technique relies on the combined radiation of an electric dipole and a magnetic dipole, which naturally produces two orthogonal field components with a 90° phase difference; the CP performance is achieved. As a result, the proposed 4 × 4 antenna array achieves a 3-dB axial ratio bandwidth (ARBW) of 24.3%. Two orthogonal microstrip patch antenna units are used in [36]. Each cell is fed with a 90° phase difference to achieve CP performance and a 3-dB ARBW of 12.2% for a 2 × 2 antenna array. A wideband high-gain CP rectenna is proposed in [38]. The circular polarization is achieved by utilizing complementary source technology to create a 90° phase difference between the electric and magnetic dipoles. Finally, an EH technique is implemented, achieving a wide impedance bandwidth of 36.8%, a wide ARBW of 29.54%, a peak gain of 8.5 dBic, and an efficiency of 61%. Although the above CP antenna arrays have been used in WPT/EH, their narrower ARBW do not allow for good CP performance, and they have not been demonstrated in SWIPT. In summary, it is necessary to design a CP antenna array with high gain, wide ARBW, and an asymmetric PD with low loss suitable for mmWave SWIPT applications.

In this article, a design of asymmetric power division and system integration for mmWave SWIPT is proposed. Here, two types of asymmetric PDs are proposed. The first is a substrate-integrated waveguide (SIW) asymmetric PD, which achieves unequal power division by altering the electromagnetic field distribution in the coupling region through the introduction of a metallized via. The second one is a Wilkinson-type PD, where the power division ratio can be adjusted by modifying the impedance of its branches. Both PDs were fabricated and experimentally evaluated, with a demonstrated power split ratio of 3:1, to compare their performance in terms of insertion loss, bandwidth, and isolation. The SIW PD operates at 25.36–31.36 GHz (21.15%), the isolation between the two output ports is better than −10 dB, and the total loss in the operating frequency band is about 2.02 ∼ 2.34 dB. The Wilkinson PD operates in the 20–40-GHz (66.6%) band and the measured isolation of the two output ports is better than −14.6 dB, with a total loss of 1.08 ∼ 1.24 dB. The test results show that the Wilkinson asymmetric PD exhibits excellent performance in terms of wide bandwidth, low loss, simple structure, and compact size, making it a suitable choice for SWIPT applications. In order to reduce the multipath effect and polarization loss, a wideband, high-gain CP 4×4 receiving antenna array is proposed. The measured operating band of the array antenna is 23.6–34 GHz (36.1%), and the 3-dB ARBW is 24.2–32.8 GHz (30.2%). Moreover, the gain in the operating band is greater than 18 dBi, the flatness of the gain is less than 1 dB, and the peak gain is 19.6 dBic. Finally, the proposed Wilkinson unequal PD, 4 × 4 CP antenna array, and rectifier were integrated. Both the WPT and the performance of information transmission were measured.

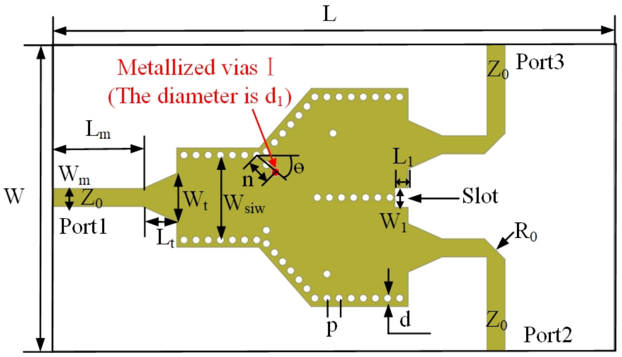

Fig. 2. Structure of the proposed asymmetric SIW PD. L = 46.4 mm, W = 25.3 mm, W_m = 1.5 mm, L_m = 7.5 mm, W_t = 4.0 mm, L_t = 2.8 mm, W_{SIW} = 7.0 mm, n = 2.0 mm, = 40°, d = 0.6 mm, d_1 = 0.6 mm, p = 1.5 mm, R_0 = 1.7 mm, W_1 = 2.5 mm, and L_1 = 1.5 mm. (The above parameter values are when the power division ratio is 3:1.)

This article is organized as follows. Section II details the structure and design principles of the asymmetric PD and also gives the measured results. The structure, operation principle, and measured results of the wideband CP antenna are discussed in Sections III and IV. The demonstration of the SWIPT system is given in detail in Section IV. Finally, Section V gives a summary.

II. ASYMMETRIC PD DESIGN

A. Asymmetric SIW Unequal PD

The structure of the proposed asymmetric SIW PD is shown in Fig. 2 (here denoted as PD I) with an overall dimension of $L \times W \times H$ ($4.3 \times 2.3 \times 0.047\ \lambda_0^3$), which consists of a single-layer Rogers-RT Duroid 5880 ($\varepsilon_r = 2.2$ and $\tan\delta = 0.0009$) dielectric substrate, rows of sidewall metallized vias, and two copper layers. Here, a microstrip line transition to a tapered line is used to improve impedance matching for all three ports. The Y-shaped branch is used to design the coupling area, and a metallized through hole is introduced into the side of the coupling area near port 3. The arrangement and location of metallized vias I can affect the electric field distribution in the coupling area, so as to control the power distribution of the output port. Rectangular slots between output ports 2 and 3 are introduced to help improve the isolation between the two ports. Due to the large size of the mmWave connector, it is difficult to test if the distance between the output ports is close, so the microstrip lines of ports 2 and 3 are curved by 90°.

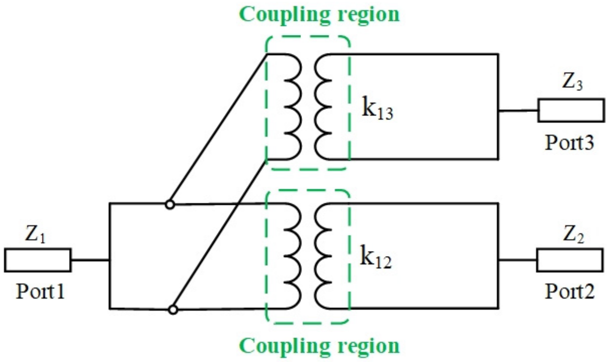

Fig. 3. Equivalent circuit of asymmetric SIW PD.

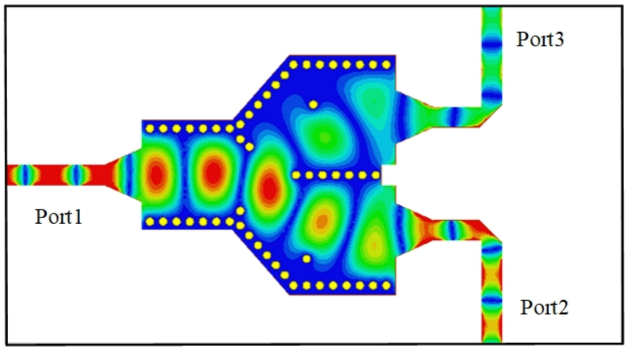

Fig. 4. Electric field distribution of asymmetric SIW PD at 28 GHz.

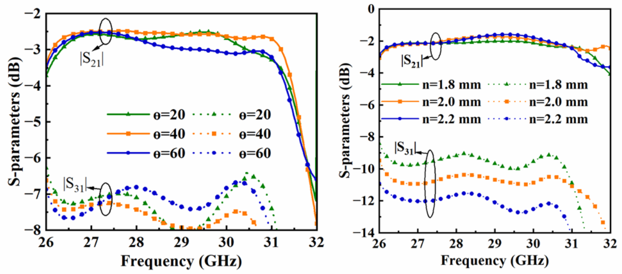

(a) (b)

Fig. 5. Power ratio of the proposed asymmetric SIW PD with different parameters. (a) Different values of θ. (b) Different values of n.

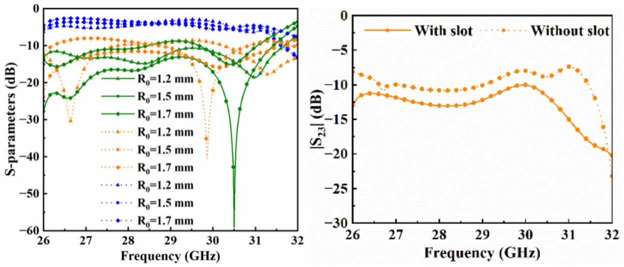

(a) (b)

Fig. 6. Performance of the proposed asymmetric SIW PD with different parameters. (a) Reflection coefficients for different values of R_0 (the green line is $|S_{11}|$, the yellow line is $|S_{22}|$, and the purple line is $|S_{33}|$). (b) Isolation behavior for the case with and without the slot.

This operation not only reduces the coupling and improves the isolation between the two output ports but also meets the mmWave connector assembly requirements. The bend of the microstrip line is chamfered, which helps to optimize current distribution and reduce signal reflection and transmission loss.

In order to reduce the leakage of electromagnetic waves from the SIW cavity, the radius d of the metallized vias as well as the distance p between the centers of two adjacent metallized vias should satisfy $d/p \leq 0.5$ and $d/\lambda_0 \geq 0.1$, where λ_0 is the wavelength of the operating frequency in free space. The frequency of the SIW resonant cavity mode T_{mnl} can be calculated using the following equations [39]:

$$f_{mnl} = \frac{1}{2\sqrt{\mu\varepsilon_r}}\sqrt{\left(\frac{m}{W_{\text{eff}}}\right)^2 + \left(\frac{n}{L_{\text{eff}}}\right)^2 + \left(\frac{l}{h}\right)^2} \quad (1)$$

$$W_{\text{eff}} = L_1 - 1.08\frac{d^2}{p} + 0.1\frac{d^2}{L_1} \quad (2)$$

$$L_{\text{eff}} = L_2 - 1.08\frac{d^2}{p} + 0.1\frac{d^2}{L_2} \quad (3)$$

where ε_r and μ are the permittivity and permeability of the substrate, respectively; m, n, and l are the number of variations of the standing wave along the x-, y-, and z-axes, respectively; and W_{eff}, L_{eff}, and h are the length, width, and height of the equivalent resonant cavity, respectively. The SIW resonant cavity in this work operates in the TE_{10} mode.

The equivalent circuit of the proposed asymmetric SIW PD is shown in Fig. 3. Z_1–Z_3 are the input impedances of the three ports, which are 50 Ω here. The coupling coefficients of the coupling regions of the two output ports are k_{12} and k_{13}. The number of metallized vias introduced and the distance from the rows of sidewall metal vias affect the coupling coefficients between the two output paths, and the power ratio between the two output ports is changed. We also explore the electric field distribution of the proposed asymmetric SIW PD at 28 GHz, as shown in Fig. 4. From the electric field distribution, it can be seen that the introduction of the metal vias changes the energy distribution between the two outputs, and different power distribution ratios are obtained.

It is possible to design a PD with different ratios by adjusting the number of metallized vias and the distance from the sidewall, respectively. Here, we take the power ratio of 3:1 as an example to explore the performance of this asymmetric SIW PD. The effect of the angle of rotation of the metallized via I for $|S_{21}|$ and $|S_{31}|$ is shown in Fig. 5(a). When the angle of rotation is increased from 20° to 60°, $|S_{21}|$ exhibits only a slight change, whereas $|S_{31}|$ shows a more pronounced variation. It shows that the power ratios of the two output ports change with the angle of rotation. Similarly, the distance n between the metallized via I and the sidewall metallized via array is also explored, and the simulation results are plotted in Fig. 5(b). When the value of n is changed, the change of $|S_{21}|$ is small and $|S_{31}|$ changes significantly, so the power magnitude of the two output ports can be realized by adjusting the value of n. When exploring the variations of the above two parameters, all other parameters are fixed at their optimized values, which are summarized in the legend of Fig. 2.

Different parameters of asymmetric SIW PD are analyzed to explore their impact on performance. As can be seen from

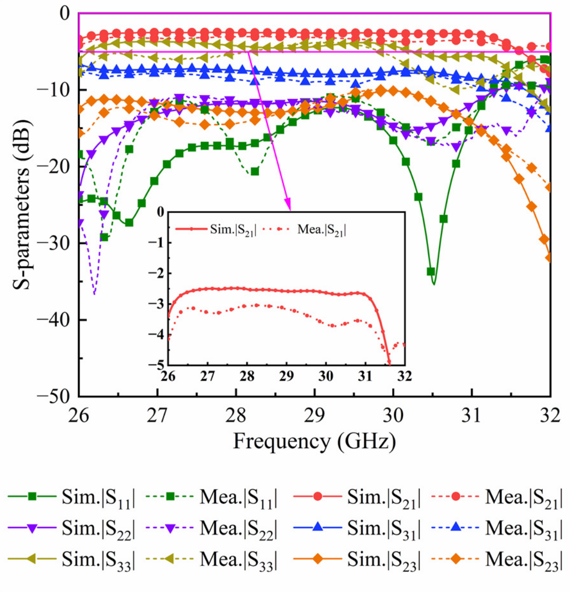

Fig. 7. Simulated and measured S-parameters of the proposed asymmetric SIW PD at a power division ratio of 3:1.

Fig. 6(a), the reflection coefficients of the three ports have large fluctuations when varying the value of the tangent angle R_0 of the corners of the two output ports. Therefore, adjusting the value of R_0 can control the impedance matching of SIW PD, and the impedance matching of the three ports is optimized when R_0 = 1.7 mm. Then, the influence of the structure with and without a slot on the isolation is analyzed in Fig. 6(b). The introduction of a slot can greatly improve the isolation between the two output ports. The final optimized dimensions of the proposed asymmetric SIW structure at a power ratio of 3:1 are shown in Fig. 2.

The above design is fabricated and measured according to the optimized size to verify the correctness of the proposed asymmetric SIW PD power ratio. Here, a power ratio of 3:1 is taken as an example. The simulated and measured S-parameter results are plotted in Fig. 7. The S-parameter region from −5 to 0 dB is zoomed in to better visualize the performance. It shows that the $|S_{11}|$ and $|S_{22}|$ simulated and measured operating bands are 26–31.34 GHz (18.6%) and 26–31.92 GHz (20.4%), respectively. The system measured $|S_{21}|$ and $|S_{31}|$ are −3.27 and −8.0 dB at 27 GHz, −3.0 and −8.6 dB at 28 GHz, −3.11 and −8.9 dB at 29 GHz, and −3.5 and −8.7 dB at 31 GHz. The total losses of the two output ports of the PD at the four frequency points are 2.02, 1.94, 2.10, and 2.34 dB. The total losses of the two output ports in the operating frequency band are about 2.02 ~ 2.34 dB. Meanwhile, the simulated and measured isolation $|S_{23}|$ of the PD is also depicted in Fig. 7, which is lower than −10 dB. As shown in Fig. 7, the measured $|S_{11}|$ exhibits additional resonance dips compared with the simulated results. These discrepancies can be primarily attributed to several practical factors. First, manufacturing tolerances in substrate thickness, dielectric constant, and conductor etching may cause deviations from the ideal design parameters assumed in simulation. Second, fabrication imperfections in the SIW vias and misalignment or soldering variations of the SMA connectors can introduce additional mismatches and insertion losses. Third, measurement uncertainties, such as connector and cable losses as well as calibration errors, may further influence the measured data. Finally, nonideal effects not fully accounted for in the simulation—such as conductor surface roughness, radiation leakage, and parasitic coupling—may also contribute to the observed differences.

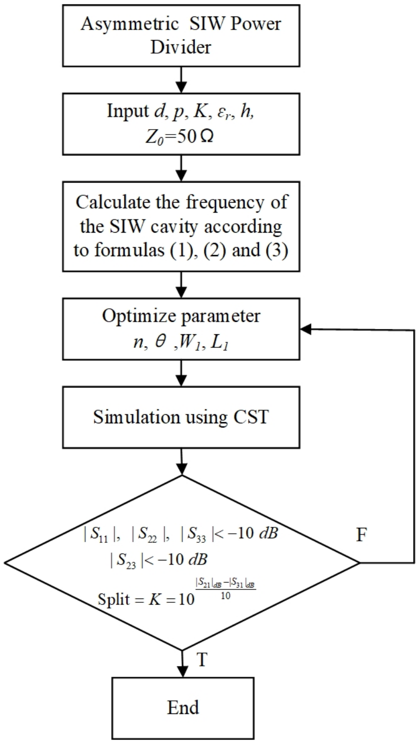

Fig. 8. Flowchart of the proposed SIW PD with different power ratios.

Despite these discrepancies, the measured results show good agreement with the simulation, thereby validating the accuracy and robustness of the proposed design.

Fig. 8 summarizes the design flowchart for different power ratios to illustrate the scalability of the proposed SIW PD.

B. Asymmetric Wilkinson PD

The topology of the proposed asymmetric Wilkinson PD is shown in Fig. 9 (here as PD II). It consists of a single layer of Rogers-RT Duroid 5880 substrate and two layers of copper, with overall dimensions of $L \times W \times H$ $(2.17 \times 2.0 \times 0.025\lambda_0^3)$. The input signals from port 1 go to ports 2 and 3. The isolation resistors between the output ports are used to increase isolation. All three ports are connected with a 50-Ω impedance. A two-stage impedance transformation approach is used to extend the operating bandwidth of the PD, and asymmetrical transmission lines are designed in order to achieve different power ratios.

The odd–even mode analysis can be used to analyze the characteristic impedance and power ratio of the PD. The asymmetric Wilkinson PD can be regarded as the superposition of the even-mode equivalent circuit and the odd-mode equivalent circuit, and the equivalent circuit diagram is shown in

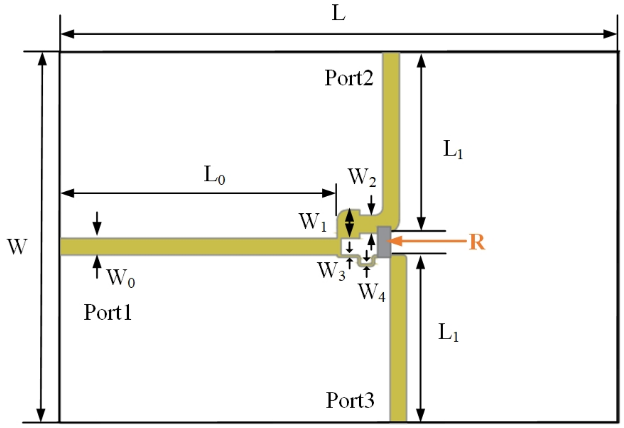

Fig. 9. Topology of the proposed asymmetric Wilkinson PD. W = 20 mm, L = 21.7 mm, W_0 = 0.64 mm, L_0 = 10.75 mm, W_1 = 1.1 mm, W_2 = 0.7 mm, W_3 = 0.1 mm, W_4 = 0.1 mm, L_1 = 6.5 mm, and R = 150 Ω. (The above parameter values are when the power division ratio is 3:1.)

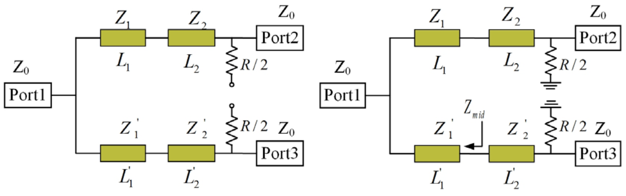

(a) (b)

Fig. 10. Equivalent circuits in different modes. (a) Even mode. (b) Odd mode.

Fig. 10(a) and (b). Z_0 is the characteristic impedance of the three ports (here, the characteristic impedance Z_0 is matched to 50 Ω), Z_1, Z_1', Z_2, and Z_2' are the cascaded characteristic impedance of the two branch lines; V_2 and V_3 are the voltage of the two output ports; and k^2 is the power ratio of the output ports. According to Fig. 10(a), the central point potential of the isolation resistance in the even-mode equivalent circuit is zero, which is equivalent to an open circuit, so the characteristic impedance ratio is as follows [40]:

$$\frac{Z_2}{Z_2'} = \left(\frac{V_2}{V_3}\right)^2 = \frac{1}{k^2} \tag{4}$$

where $\frac{V_2}{V_3} = \frac{1}{k}$. For the even mode, the total input impedance of the two paths in parallel needs to be matched to Z_0

$$Z_0 = \frac{Z_2^2 \cdot (Z_2')^2}{Z_0(Z_2^2 + (Z_2')^2)} \tag{5}$$

so

$$Z_2 = Z_0\sqrt{\frac{1}{1+k^2}} \tag{6}$$

$$Z_2' = Z_0\frac{k}{\sqrt{1+k^2}} \tag{7}$$

The equivalent circuit of the odd mode is shown in Fig. 10(b), where the isolation resistor is split into two halves in parallel between the transmission lines. Then, the input impedance of a quarter of the transmission line for ports 2 and 3 is as follows:

$$Z_0 = \frac{Z_2^2}{R/2} \tag{8}$$

$$Z_0 = \frac{(Z_2')^2}{R/2} \tag{9}$$

The resistance of the isolation resistor is

$$R = \frac{2Z_0}{1+k^2} \tag{10}$$

At the first stage, impedance transformation

$$Z_1 = Z_1' = \sqrt{Z_0 Z_{\text{mid}}} \tag{11}$$

where $Z_{\text{mid}} = Z_0\sqrt{1+k^2}$, in which Z_{mid} is the impedance between stage one and stage two.

The value of L_i (i = 1, 2, 3, 4) in both modes can be calculated using the following formula:

$$L_i = \frac{\lambda}{4} \tag{12}$$

where λ is the wavelength of the center frequency.

The above analysis shows that the odd–even mode theory can calculate the transmission impedance of the asymmetric PD, and the odd mode theory can calculate the isolation resistance value. Therefore, different proportions of asymmetric PDs can be obtained.

The 3:1 power division ratio is taken as an example to verify the accuracy of the above theory, and the final optimized size is placed in Fig. 9. After that, we explore the influence of key parameters on the performance of the asymmetric PD. Fig. 11 shows that adjusting the linewidth of the transition line can change the impedance value and thus adjust the power ratio of the two output ports. When the parameters W_1 = 1.1 mm, W_2 = 0.7 mm, and W_3 = 0.1 mm, the power ratio of the two output ports is 3:1, and the impedance values are Z_1 = 37.63 Ω, Z_2 = 51.13 Ω, and Z_3 = 123.23 Ω. The isolation between the two output ports can be adjusted by changing the resistance value of the isolation resistor, and the results are shown in Fig. 12(a). Finally, the optimal isolation resistor value is determined to be R = 150 Ω. Due to the large size of the mmWave connector, the microstrip line length of the three ports is extended to facilitate the PD test, and the length of the microstrip line also affects the insertion loss of the PD. The effects of the microstrip line length L_0 are investigated, and the results are shown in Fig. 12(b). The results show that the insertion loss increases when the length of the microstrip line is prolonged. Finally, the size of L_0 was optimized to 10.75 mm.

A power ratio of 3:1 is taken as an example, the simulated and measured S-parameters are shown in Fig. 13, and the measured results are in good agreement with the simulation in HFSS. The measured operating band is 20–40 GHz ($|S_{11}| < -10$ dB), and it has good transmission efficiency and small loss in the operating band. It is noted that the values of the insertion losses $|S_{21}|$ and $|S_{31}|$ will gradually decrease as the frequency increases, mainly due to the loss of the dielectric material increasing with the frequency. Here, the measured $|S_{31}|$ and $|S_{21}|$ are −2.66 and −6.8 dB at 26 GHz, −2.52 and −6.66 dB at 28 GHz, and −2.5 and −6.62 dB at 30 GHz, respectively.

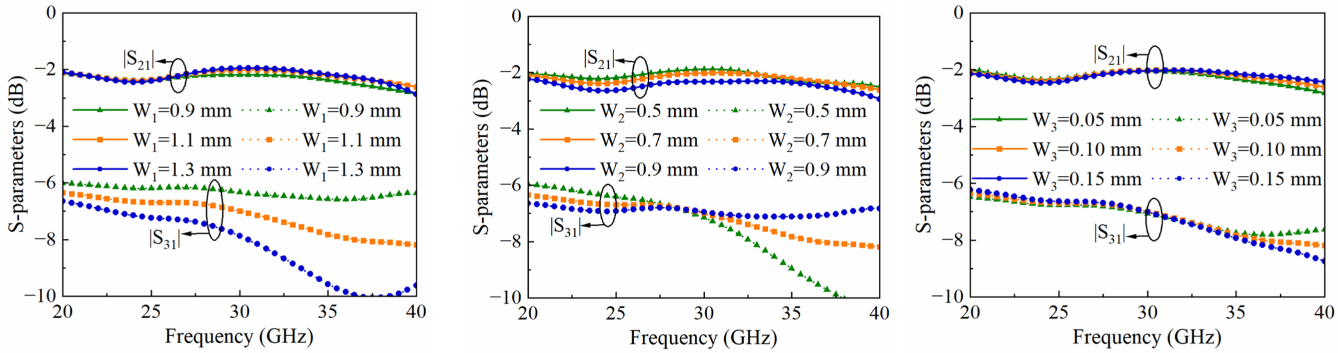

(a) (b) (c)

Fig. 11. Power ratio of the proposed asymmetric Wilkinson PD for different line widths. (a) W_1. (b) W_2. (c) W_3.

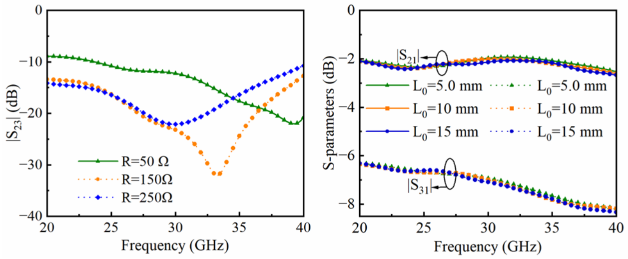

(a) (b)

Fig. 12. Performance of the proposed asymmetric Wilkinson PD with different parameters. (a) Isolation at different resistance values. (b) Insertion loss for different microstrip line lengths at the port.

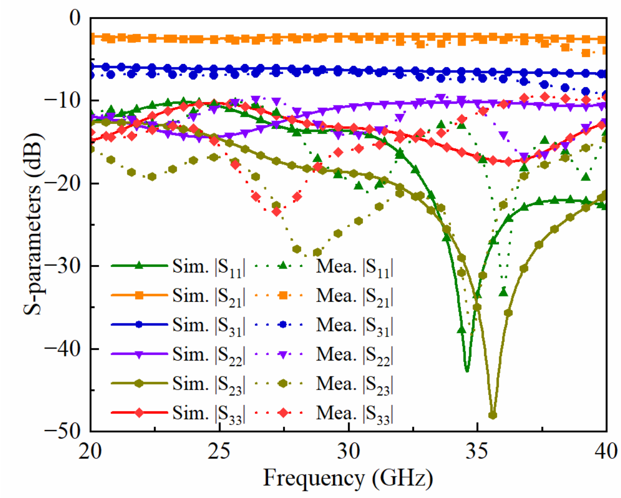

Fig. 13. Simulated and measured S-parameters of the proposed asymmetric Wilkinson PD at a power division ratio of 3:1.

The total losses of the two output ports of the PD at the three frequency points are 1.24, 1.09, and 1.08 dB. The total losses of the two output ports in the operating frequency band are about 1.08 ∼ 1.24 dB. The isolation of the measured is better than −15 dB. Eventually, the 3:1 power ratio is realized.

This Wilkinson PD can operate at different power ratios and frequency bands, and its general working flow diagram is summarized in Fig. 14.

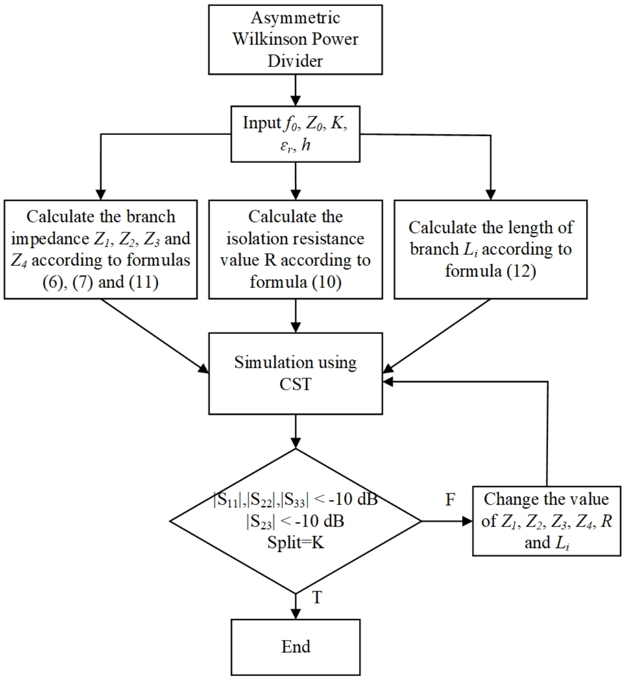

Fig. 14. Flowchart of the proposed Wilkinson PD with different power ratios.

C. Comparison and Discussion

The above two proposed designs have good performance and an adjustable power division ratio. In mmWave SWIPT systems, the performance of PDs—such as insertion loss, isolation, and bandwidth—directly affects the signal-to-noise ratio (SNR) at the communication port and the RF-to-dc conversion efficiency at the energy port. Therefore, the measured performances of the two PD designs are summarized in Table I to highlight the tradeoffs in their suitability for SWIPT integration. Here, total losses represent the total insertion losses, including conductor losses, radiation losses, and dielectric losses. As a demonstration, we selected the total insertion loss value of the two PDs at 28 GHz, which can be calculated using the following equation [41]:

$$\text{TotalLoss} = -10\log_{10}^{(|S_{21}|^2+|S_{31}|^2)} \tag{13}$$

TABLE I
COMPARISON OF THE PERFORMANCE OF PDs I AND II

PD	Freq. (GHz)	Isolation (dB)	Total Loss (dB)	Size (λ_0^3)
I	26−31.34	< −10	1.94	4.3×2.3×0.047
II	20−40	< −15	1.09	2.17×2.0×0.025

PD I is the SIW power divider, PD II is the Wilkinson power divider. The total loss is calculated at 28 GHz.

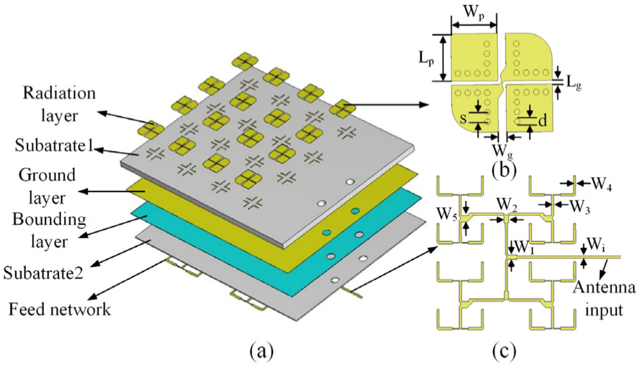

Fig. 15. Proposed 4 × 4 CP antenna array. (a) Configuration. (b) Element radiation layer. (c) Feed network. W_p = 2.39 mm, L_p = 2.44 mm, W_g = 0.42 mm, L_g = 0.2 mm, s = 0.5 mm, d = 0.3 mm, W_i = 0.53 mm, W_1 = 1.11 mm, W_2 = 1.05 mm, W_3 = 0.5 mm, W_4 = 0.46 mm, and W_5 = 1.44 mm.

It can be seen from the table that PD II (asymmetric Wilkinson PD) is better than PD I (asymmetric SIW PD) in terms of operating band bandwidth, isolation, total loss between two output ports, and structure size. Therefore, PD II is selected for SWIPT.

III. RECEIVING ANTENNA AND RECTIFYING CIRCUIT

A. 4 × 4 *Receiving Antenna Array*

Wideband, high-gain, CP receiving antennas are of great value in SWIPT applications. First, the characteristics of circular polarization can effectively overcome the polarization mismatch problem in the multipath propagation environment and maintain stable EH efficiency and communication quality when the attitude of the receiver changes randomly. It significantly improves the robustness of the system. Second, the high gain of the antenna array not only enhances the directivity and energy transmission ability of the antenna but also expands the effective coverage of the system. Moreover, it can support longer distance WPT. The suppression effect of CP waves on multipath interference also reduces signal attenuation and further improves the transmission efficiency of energy and information. These properties make CP high-gain antennas particularly suitable for SWIPT in complex environments.

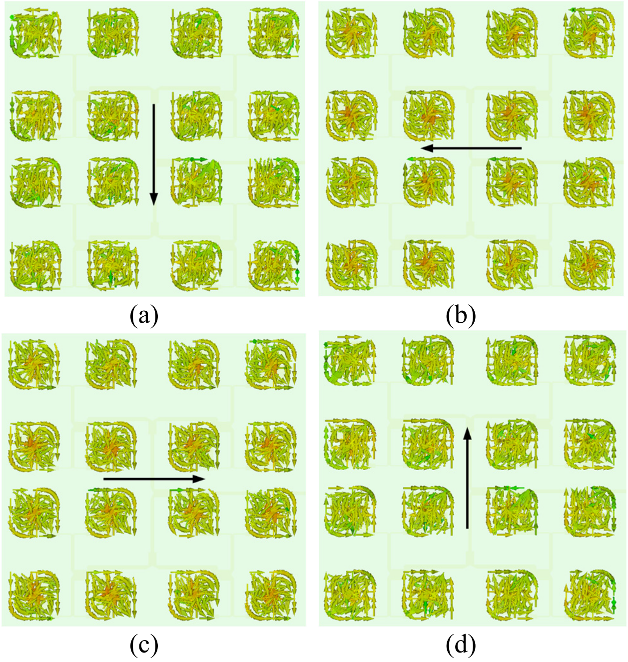

Fig. 16. Surface current of the proposed 4 × 4 CP antenna array at 28 GHz. (a) t = 0. (b) t = $T/4$. (c) t = $T/2$. (d) t = $3T/4$. (T is the period of the oscillation.)

The proposed CP antenna array structure is shown in Fig. 15(a). Two layers of Rogers RT 5880 substrate were bonded together to form a CP antenna array. The thicknesses of substrates 1 and 2 were 3.175 and 0.508 mm, respectively, and the material of the bonded layer was RO4450F ($\varepsilon_r = 3.52, \tan\delta = 0.004$, and $h = 0.1$ mm). The 4 × 4 radiation elements of this antenna array are placed on the top layer of substrate 1, and the bottom layer of substrate 1 is the radiation slot coupling layer (ground layer). A feeding network with 16 channels of equal amplitude and phase is placed at the bottom of substrate 2 to feed each antenna element. Each stage of the feeding network is composed of T-type PDs, as shown in Fig. 15(c). The port of the antenna is impedance matched at 50 Ω; then, the impedance is matched by a quarter impedance converter, and the energy is evenly distributed to the feeders of each element. After that, the energy is coupled to the groove of the formation and excited to the radiation of each element. The radiation element structure diagram is shown in Fig. 15(b), where each radiation element consists of four patches, two of which are connected by metal strips with two circular holes dug out. Two perpendicular linearly polarized (LP) ME dipoles are excited to achieve circular polarization. The surface current of the 4 × 4 antenna array at 28 GHz is analyzed to illustrate the circular polarization, as shown in Fig. 16. At different instants, the antenna surface current circulates counterclockwise, which is represented by right-handed circular polarization (RHCP). Thus, the antenna array generates RHCP complementary source radiation in the $+z$-direction.

The antenna array was fabricated and measured. As shown in Fig. 17, the measured results are in good agreement with the simulation ones, the measured −10-dB impedance bandwidth is 36.11% in the 23.6–34 GHz, and the simulated −10-dB impedance bandwidth is 36.14% in the 23.8–34.3 GHz. There is a 30.2% measured 3-dB ARBW over the band ranging

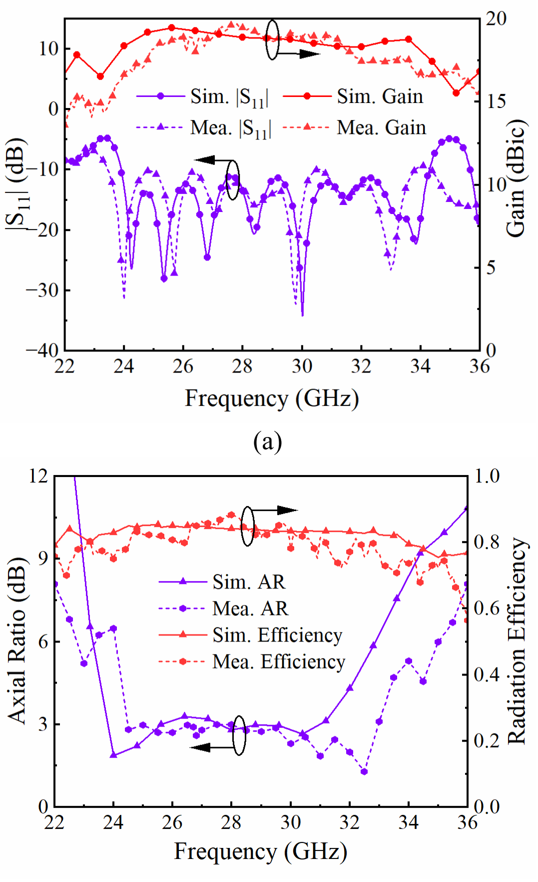

(a)

(b)

Fig. 17. Measured and simulated results of the proposed 4 × 4 CP antenna array. (a) Reflection coefficient and the realized gains. (b) Axial ratio and radiation efficiency.

from 24.2 to 32.8 GHz and a 28% simulated 3-dB ARBW over the band ranging from 23.8 to 31.5 GHz. The 3-dB gain bandwidth of the array covers the operating band, and the peak gain measured is 19.6 dBic. The small difference between the measured and simulated results can be attributed to the coaxial transmitter connectors, losses in the bonding layer, and higher-than-expected dielectric losses. Fig. 18 shows the measured and simulated normalized gain plots for the array at 26, 28, and 30 GHz. It shows that a sidelobe of about −15 dB is achieved over the operating frequency band. In addition, there are some subtle differences between the results of measurement and simulation due to manufacturing errors and testing errors.

B. High Conversion Efficiency Rectifying Circuit

As an important part of WPT, the performance of the rectifying circuit affects the RF-to-dc conversion efficiency of the system. The proposed rectifying circuit structure is placed in Fig. 19, including the rectifier diode, sector filter, and load. The rectifying circuit is printed on a Rogers RT5880 substrate, which is the same substrate as the CP receiving antenna. Here, a GaAs flip-chip Schottky diode, model MA4E1317, is used, which can operate at frequencies up to 80 GHz [42]. Diodes with high breakdown voltage (V_{br} = 7V), low zero bias junction capacitance (C_{j0} = 0.02 pF), low threshold voltage (V_{bi} = 0.7V), and small series resistance (R = 4Ω) are connected in parallel with the rectifying circuit. For diodes in parallel, the threshold voltage has little impact on the performance of the circuit, but it helps to reduce the inherent internal power loss of the diode resistance and enhance the power handling ability [43]. The characteristic of the rectifying circuit structure is that the matching circuit is composed of only one microstrip branch, which greatly simplifies the complexity of the structure and improves the RF-to-dc conversion efficiency. As a bypass capacitor, the fan filter can not only suppress the harmonics but also smooth the voltage ripple in the dc output section. The design offers several advantages, including improved harmonic suppression, minimized distortion, and reduced loss.

When the rectifier circuit is simulated and optimized, its input impedance is not only 50 Ω. The specific process is to use CST to extract the impedance of the port with more output power of the Wilkinson PD, export the SNP file, and then import it into ADS for cosimulation to describe the overall conjugate matching process [38]. This process can approximate the integration of the divider and the rectifier (described as codesigned), and the conjugate matching process can match the divider and the rectifier with minimum loss.

The RF-to-DC conversion efficiency of the rectifying circuit can be expressed as [24]

$$\text{Eff} = \frac{V_{\text{dc}}^2}{P_{\text{in}} R_{\text{load}}} \times 100\% \tag{14}$$

where V_{dc} is the output dc voltage of the load resistor R_{load} and P_{in} is the input power of the rectifying circuit.

The performance of the proposed rectifier is verified, and the conversion efficiency of the rectifier for different input signals at 28 GHz is also listed in Fig. 20. The figure shows that the conversion efficiency of QPSK signal is lower than that of continuous wave (CW) signal in the input power range of −10 to 30 dBm, and the highest simulated and measured RF-to-dc conversion efficiency of QPSK is 52.56% and 47.73%. Compared with CW and QPSK, the conversion efficiency of OFDM signal is higher than that of CW signal at low input power, and the conversion efficiency of OFDM signal is lower than that of CW signal at high input power, which is consistent with the nonlinear behavior of the rectifier. The highest measured conversion efficiency of QFDM is 45.7%. Therefore, the measured peak efficiency of the rectifier is always greater than 45% under the excitation of both CW signal and modulated signals, which proves the excellent performance of the proposed rectifier.

The proposed rectifying circuit is fabricated and measured, and its measured frequency band operates from 22 to 32.5 GHz with $|S_{11}| < -10$ dB in Fig. 21. The corresponding optimal load resistance load value is 100 Ω, and the optimal input power is 18 dBm, and the RF-to-dc conversion efficiency from 24- to 31-GHz band is greater than 50% in the operating frequency band. The maximum conversion efficiency value of 60.5% is achieved at 24 GHz. In comparison with the simulation, the shift of the peak efficiency to 24 GHz can be ascribed to fabrication tolerances, insertion losses associated with

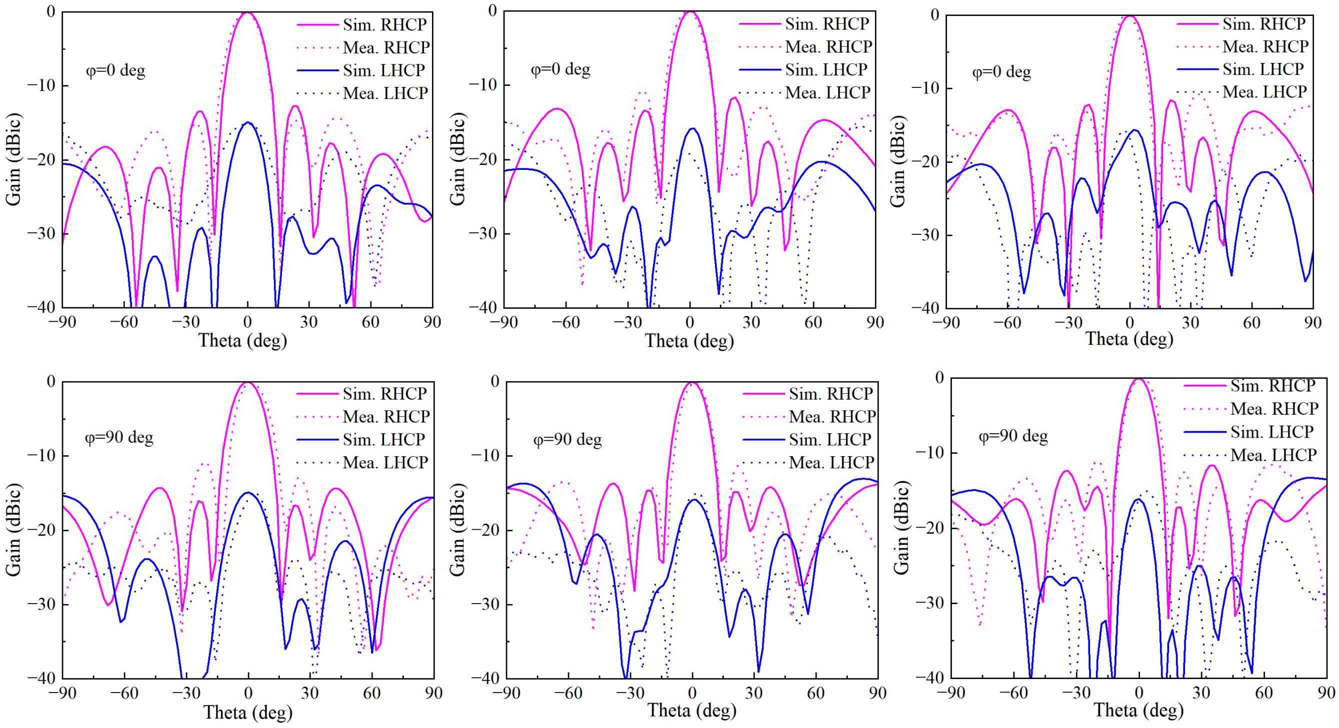

(a) (b) (c)

Fig. 18. Simulated and measured normalized pattern of the proposed 4 × 4 CP antenna array. (a) 26 GHz. (b) 28 GHz. (c) 30 GHz.

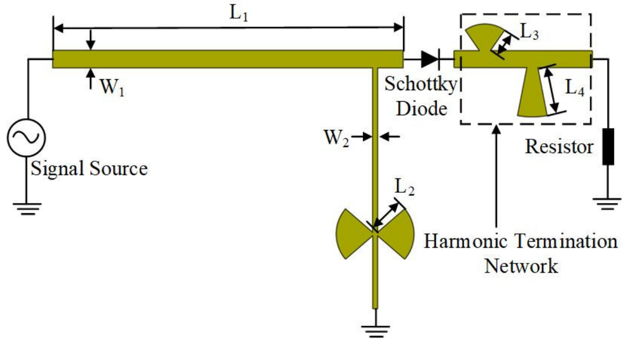

Fig. 19. Proposed rectifier circuit structure. $L_1 = 8$ mm, $W_1 = 0.64$ mm, $L_2 = 1.3$ mm, $W_2 = 0.18$ mm, $L_3 = 0.91$ mm, and $L_4 = 1.77$ mm.

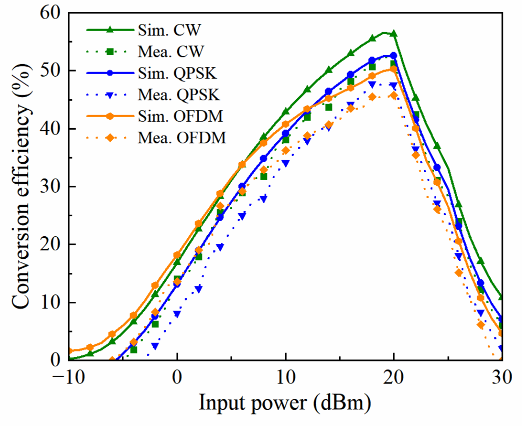

Fig. 20. Simulated and measured rectifier performance of CW, QPSK, and OFDM transmitted signals at 28 GHz.

connectors, cables, and calibration accuracy during measurement, as well as mismatches between the practical diode packaging and its equivalent simulation model. Therefore, the rectifying circuit has the advantages of simple structure, high RF-to-dc conversion efficiency, easy integration, and wide frequency band, which is more suitable for SWIPT.

IV. SWIPT SYSTEM INTEGRATION AND MEASUREMENT

A high-gain CP receiving antenna, an asymmetric Wilkinson PD, and a high-efficiency rectifying circuit are integrated as the SWIPT system, as shown in Fig. 22(a). Since the PD is asymmetric, the two asymmetric ports are connected to the WPT and WI. The port of the 4 × 4 high-gain CP antenna array is connected to port 1 of the asymmetric Wilkinson PD, port 2 (with power P_{in2}) is connected to the input port of the rectifying circuit, and port 3 (with power P_{in3}) is connected to the communication device. Therefore, P_{in2} and P_{in3} are as follows [9]:

$$P_{\text{in2}} = \frac{k^2}{1+k^2}P_r, P_{\text{in3}} = \frac{1}{1+k^2}P_r \qquad (15)$$

where P_r is the received power of the receive antenna, expressed by [44]

$$P_r = \frac{P_t G_t G_r \lambda^2 \eta_a}{(4\pi)^2 D^2} \qquad (16)$$

where P_t and P_r are the transmit power and receive power of the antenna, respectively; G_t and G_r are the gains of the

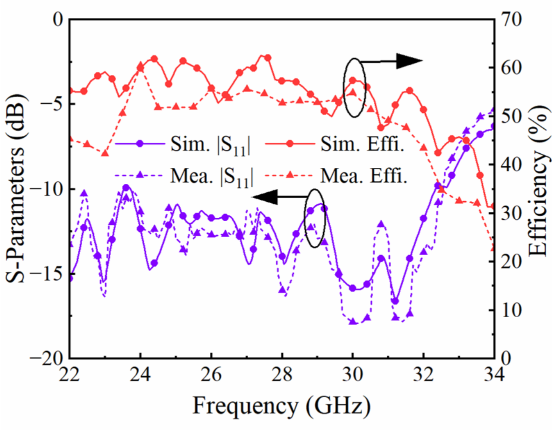

Fig. 21. Measured and simulated S-parameters and RF-to-dc conversion efficiency of the proposed rectifying circuit.

transmit and receive antennas, respectively; λ is the wavelength in free space; and η_a is the efficiency of the antenna. D is the distance between the transmit and receive antennas. The RF-to-DC conversion efficiency in (14) is as follows:

$$\mathrm{Eff} = \frac{(4\pi)^2\, L^2 V_{\mathrm{dc}}^2}{P_t G_t G_r \eta_a \lambda^2 R} \cdot \frac{1+k^2}{k^2} \tag{17}$$

All the above ports are integrated together to achieve good impedance matching. This integration reduces the reflection loss, connector insertion loss, and cable loss in the SMA interface connection, reduces the instability caused by multi-module splicing, and reduces the size of the overall structure. The test setup for WPT to data communication is depicted in Fig. 22(b). It includes a vector signal generator (VSG), a horn antenna (HZ23121801-1901), a power amplifier with a gain of 40 dB, an integrated structure (including 4 × 4 CP antenna array, asymmetric Wilkinson PD, and rectifying circuit), a vector signal analyzer (VSA), and a BQ25504 dc–dc battery management unit and multimeter. The VSA generates CW and modulated wave (here, FM wave as an example), and the RF wave is amplified by the amplifier and excited by the horn antenna. The 4 × 4 CP receiving antenna array receives the RF wave transmitted by the horn antenna at a distance of D (D = 1.6 m). At the rectifier port of WPT, the power management unit is connected to the rectifying circuit for stabilizing the dc output voltage. The voltmeter is used to test the output voltage at the load resistor of the rectifying circuit. The VSA is used to connect the communication ports for evaluating the quality of wireless transmission.

At the rectifier port, the signal generator is used to transmit CW signal to test the power distribution at the output ports of the PD, which is shown in Fig. 23. The rectifier port accounts for about 75% of the total input power, and the communication port accounts for about 25% of the power, so the designed 3:1 power ratio is verified. In the communication port, the VSG generates a CW signal and an FM signal to verify the communication quality of wireless data. Taking the FM signal as an example, the FM signal received by the spectrum analyzer from the communication port is shown in Fig. 24(b).

TABLE II
COMPARISON OF THE INFLUENCE OF DIFFERENT POWER DIVISION RATIOS ON SYSTEM PERFORMANCE

Power Ratios	Parameters (mm)				Input Power of Rectifier (dBm)	SNR (dB)
	W_1	W_2	W_3	W_4		
1:1	0.4	0.4	0.4	0.4	16.46	60.57
2:1	1.0	0.6	0.2	0.35	17.50	58.68
3:1	1.1	0.7	0.1	0.1	17.51	56.70
4:1	1.3	0.9	0.05	0.05	17.98	54.66

The data in the table were obtained at 28 GHz.

Fig. 24 clearly shows that the FM spectrum of the received signal is almost identical to the FM spectrum of the transmitted signal. Next, we tested the SNR of the communication side under the two waveforms, as shown in Fig. 25. Compared with the transmitted signal, the CW signal and FM signal both obtain a high SNR higher than 56 dB at 26–30 GHz. The SNR of the CW signal is 58.3–61.2 dB, the SNR of the FM is 56.4–59.5 dB, and the SNR of the CW signal is higher than that of the FM signal. Therefore, the proposed design can well meet the requirements of modern communication. Here, the SNR can be calculated using the following formula [9]:

$$\mathrm{SNR(dB)} = P_{\mathrm{signal}}(\mathrm{dBm}) - P_{\mathrm{noise}}(\mathrm{dBm}) \tag{18}$$

Several power ratios—1:1, 2:1, 3:1, and 4:1—for the Wilkinson PD were parameterized, as summarized in Table II. As shown in the table, increasing the power division ratio results in a higher input power at the rectifier port, while the communication-side power and corresponding SNR gradually decrease. These results clearly demonstrate the tradeoff between power transfer and communication quality. A larger asymmetry ratio enhances power transmission, whereas a smaller ratio maintains a higher SNR, which consistently remains above 54 dB. More importantly, the proposed design allows flexible adjustment of the power ratio, enabling optimization for different application requirements.

The measured performance of each module in the SWIPT system is listed in Table III to show the excellent performance of the proposed work. The table shows the high total efficiency and high gain of the proposed CP antenna array, the lower losses of the Wilkinson PD, and the high conversion efficiency of the rectifier. The total efficiency of the system is calculated by the following equation:

$$\eta_{\mathrm{System}} = \eta_A \times \eta_P \times \eta_R \tag{19}$$

where η_{System} is the overall efficiency of the integrated system, η_A is the total efficiency of 4 × 4 CP antenna array, η_P is the transmission efficiency of the Wilkinson PD, and η_R is the RF-to-dc conversion efficiency of the rectifier.

In order to fully illustrate the advantages of the proposed work, some rectennas with advanced performance published recently are compared, as shown in Table IV. Compared with the existing advanced works, this work realizes SWIPT

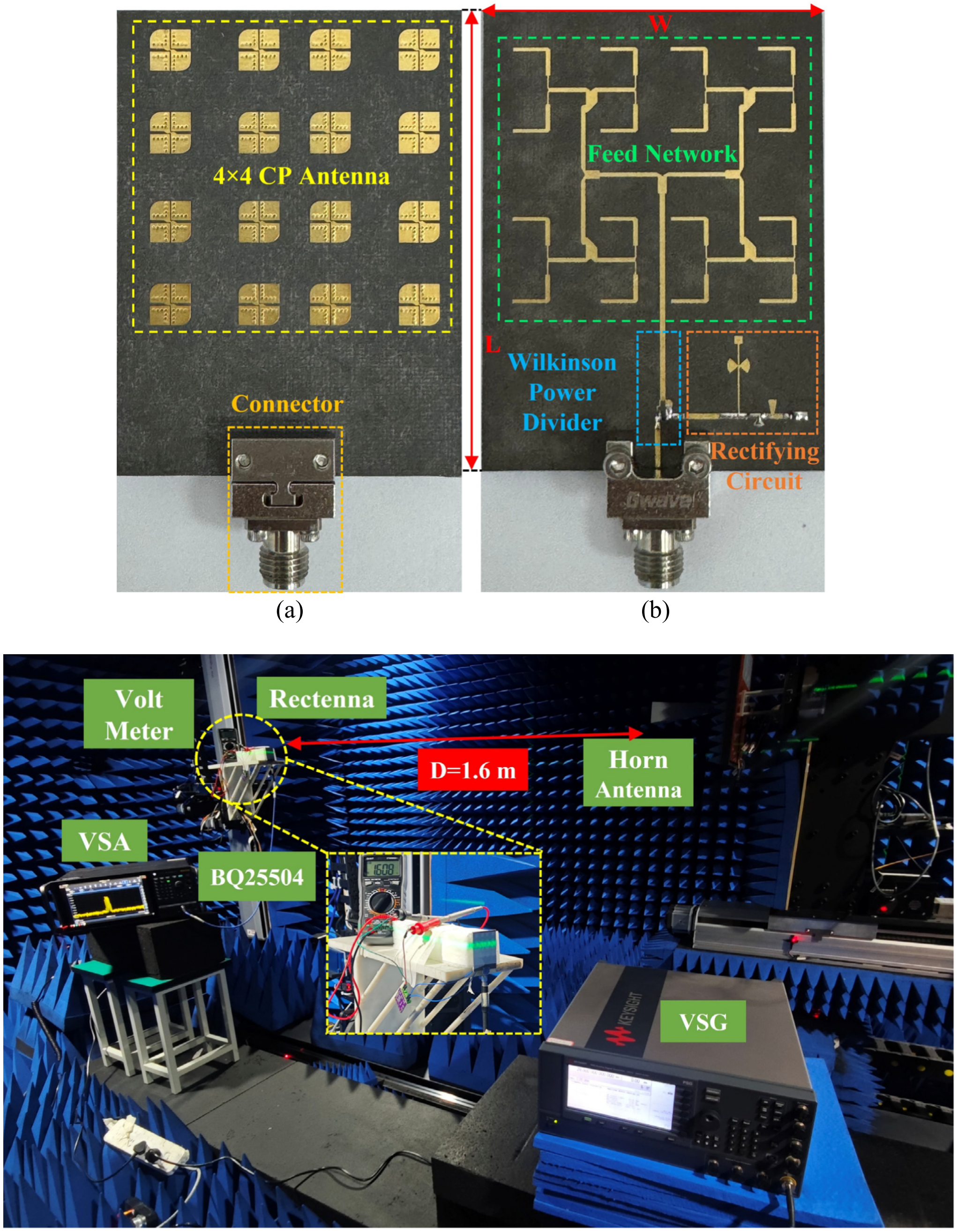

(a) (b)

(c)

Fig. 22. Fabrication and measurement. (a) Photograph of the top view of the fabricated integrated SWIPT rectenna. (b) Photograph of the back view of the fabricated integrated SWIPT rectenna. (c) Measurement of the SWIPT system. L = 58.41 mm and W = 43.46 mm.

application in the mmWave band for the first time. Although work [29] can realize WPT and WI, as a single-port antenna, it can only use a rectifying circuit and communication device alternately, which greatly reduces the flexibility of the system. In our work, the rectifying circuit and communication module are connected simultaneously, reducing system complexity and enhancing operational efficiency. In comparison, the asymmetric coupler reported in [9] achieves SWIPT functionality in the sub-6-GHz band, but the system suffers from a very narrow impedance bandwidth and low antenna gain. Moreover, its LP antenna exhibits poor anti-interference capability. A CP antenna is employed to improve polarization robustness in [11]; however, the rectenna still demonstrates low gain. Similarly, the rectenna in [15] exhibits a narrow impedance bandwidth and limited gain. It is also noteworthy that the SWIPT systems in [11] and [15] do not include measured signal transmission data, leaving their communication performance unverified. As summarized in Table IV, the proposed design achieves a broad operating bandwidth of 36.1%, a high measured antenna gain of 19.6 dBic, and a high RF-to-dc conversion efficiency of 60.5%, clearly outperforming the existing state-of-the-art works.

TABLE III
PERFORMANCE OF EACH MODULE OF THE SWIPT SYSTEM

Frequency	Antenna (4×4 CP array)		Wilkinson Power Divider		Rectifier	Overall Efficiency of the Integrated System
	Total Efficiency	Realized Gain	Total Loss	Power Split	RF-DC Conversion Efficiency	
24 GHz	79%	16.90 dBic	1.01 dB	2.70:1	60.5%@18 dBm	37.8%
26 GHz	80%	18.90 dBic	1.24 dB	2.70:1	55.6%@18 dBm	33.4%
28 GHz	81%	19.46 dBic	1.09 dB	2.67:1	52.8%@18 dBm	33.3%
30 GHz	83%	19.10 dBic	1.08 dB	2.58:1	54.9%@18 dBm	35.6%

The data in the table are measured values.

TABLE IV
COMPARISON OF MEASUREMENTS OF THE PROPOSED SWIPT WITH OTHER WORKS

Ref.	Application	Bandwidth (GHz)	RLBW (%)	Center Freq. (GHz)	Peak Gain (dBi/dBic)	Polarization	Max. Conversion Efficiency (%)	Wave Form
[9]	SWIPT	/	/	2.4	4.57	LP	70.4%@6 dBm	CW/QPSK
[11]	SWIPT	LP:4.18-6.76 CP:4.8-5.3	47.2/9.9	5.0	7.8	LP/CP	74.2%@10 dBm	/
[15]	SWIPT	5.16-5.30	2.7	5.23	4.81	LP	50.2%@5 dBm	/
[26]	WPT	/	/	24/28	17.1/17	CP	49.1%@18 dBm 47.8%@18 dBm	CW
[27]	WPT	/	/	35	14.7	LP	49.2%@31dBm	CW
[29]	WPT	34.5–35.4	2.5	35	19.2	LP	64.9@21dBm	CW
[31]	WPT	20–26.5	28	23	7.41	LP	12%@10 dBm	CW
[32]	EH	24–40	50	32	27	LP	60%@10 dBm	CW
[36]	WPT	23.5–24.5	4.1	24	12.6	CP	42%@18 dBm	CW
[37]	WPT	21–27.7	27.5	24	11.3	CP	63%@15.2 dBm	CW
This Work	**SWIPT**	**23.6–34**	**36.1**	**30.2**	**19.6**	**CP**	**60.5%@18 dBm**	**CW/FM/QPSK/OFDM**

RLBW: Return Loss Bandwidth, SWIPT: Simultaneous Wireless Information and Power Transfer, WPT: Wireless Power Transfer, EH: Energy Harvesting.

In addition, CP antennas are designed to receive incoming waves from all directions to prevent polarization mismatch. Most importantly, a PD that can adjust the power ratio is also designed to consider the principle that the power required by the rectifier port is different from that of the communication port to avoid energy waste. As a result, the RF power is reasonably allocated, that is, the circuit has a high conversion efficiency under the best power, and the wireless communication has a good communication quality. This innovative design has the advantages of a simple structure, high conversion efficiency, adjustable power ratio, and high communication quality compared to other designs.

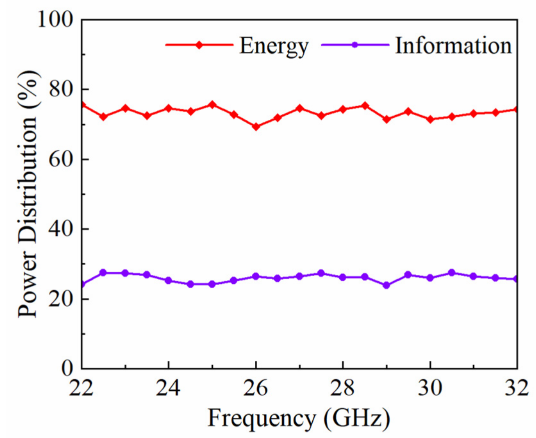

Fig. 23. Measured power distribution with different frequencies.

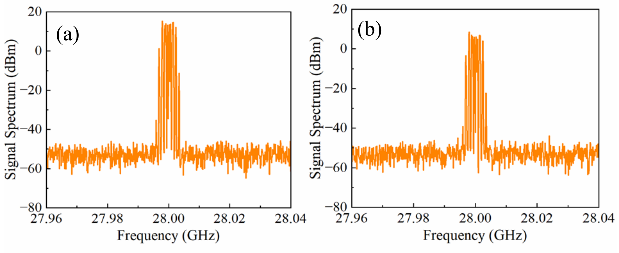

Fig. 24. Measured communication signal, FM signal, an example. (a) Transmitted signal spectrum. (b) Received signal spectrum.

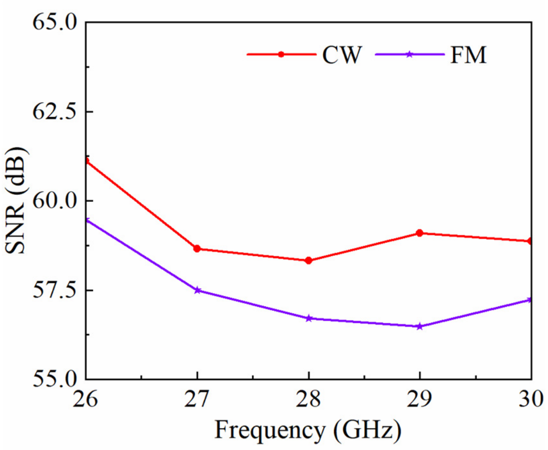

Fig. 25. Measured SNR with different frequencies for CW and FM transmitting signals.

V. CONCLUSION

In this article, an asymmetric SWIPT system operating in the mmWave band (23.6–34 GHz) is proposed and experimentally demonstrated for the first time. Two types of asymmetric PDs with adjustable power ratios are designed. The first one is an SIW PD, in which metallized vias are introduced to modify the electric field distribution at the coupling ports, thereby adjusting the output power ratio. The second one is a Wilkinson PD, in which the microstrip line impedance is varied to achieve asymmetric power division. The Wilkinson PD is selected for the SWIPT implementation due to its simple structure, low insertion loss, broad bandwidth, and compact footprint, compared with the SIW PD. In addition, a high-gain, wideband CP receiving antenna array is developed for EH, achieving a 36.1% (23.6–34 GHz) impedance bandwidth, 30.2% (24.2–32.8 GHz) ARBW, and a peak gain of 19.6 dBic. The proposed system demonstrates a 3:1 power ratio, achieving a measured RF-to-dc conversion efficiency of up to 60.5% at the rectifier port. At the communication port, the measured SNR exceeds 56 dB for both FM and CW signals, ensuring high-quality communication.

Overall, the proposed design offers adjustable power division, wide operating bandwidth, high gain, high RF-to-dc efficiency, and ease of system integration, making it highly suitable for real-time power supply and communication in mmWave electronic and IoT applications.

REFERENCES

[1] F. Xu and K. Wu, “Guided-wave and leakage characteristics of substrate integrated waveguide,” *IEEE Trans. Microw. Theory Techn.*, vol. 53, no. 1, pp. 66–73, Jan. 2005.
[2] W. C. Brown, “The history of power transmission by radio waves,” *IEEE Trans. Microw. Theory Techn.*, vol. MTT-32, no. 9, pp. 1230–1242, Sep. 1984.
[3] C.-H. Du, F. Cheng, Y. Yang, H. Zhu, and C. Gu, “Omnidirectional flexible tri-band rectenna with eliminated matching circuit for ambient RF energy harvesting,” *IEEE Trans. Microw. Theory Techn.*, vol. 73, no. 1, pp. 674–686, Jan. 2025.
[4] K. W. Choi et al., “Simultaneous wireless information and power transfer (SWIPT) for Internet of Things: Novel receiver design and experimental validation,” *IEEE Internet Things J.*, vol. 7, no. 4, pp. 2996–3012, Apr. 2020.
[5] J. O. McSpadden, L. Fan, and K. Chang, “Design and experiments of a high-conversion-efficiency 5.8-GHz rectenna,” *IEEE Trans. Microw. Theory Techn.*, vol. 46, no. 12, pp. 2053–2060, Dec. 1998.
[6] F.-J. Huang, C.-M. Lee, C.-L. Chang, L.-K. Chen, T.-C. Yo, and C.-H. Luo, “Rectenna application of miniaturized implantable antenna design for triple-band biotelemetry communication,” *IEEE Trans. Antennas Propag.*, vol. 59, no. 7, pp. 2646–2653, Jul. 2011.
[7] N. Ashraf, S. A. Sheikh, S. A. Khan, I. Shayea, and M. Jalal, “Simultaneous wireless information and power transfer with cooperative relaying for next-generation wireless networks: A review,” *IEEE Access*, vol. 9, pp. 71482–71504, 2021.
[8] R. Zhang and C. K. Ho, “MIMO broadcasting for simultaneous wireless information and power transfer,” *IEEE Trans. Wireless Commun.*, vol. 12, no. 5, pp. 1989–2001, May 2013.
[9] P. Lu, K. Huang, C. Song, Y. Ding, and G. Goussetis, “Optimal power splitting of wireless information and power transmission using a novel dual-channel rectenna,” *IEEE Trans. Antennas Propag.*, vol. 70, no. 3, pp. 1846–1856, Mar. 2022.
[10] M. Wagih, G. S. Hilton, A. S. Weddell, and S. Beeby, “Dual-band dual-mode textile antenna/rectenna for simultaneous wireless information and power transfer (SWIPT),” *IEEE Trans. Antennas Propag.*, vol. 69, no. 10, pp. 6322–6332, Oct. 2021.
[11] C. Cao, X. Zhang, C. Song, A. Georgiadis, and G. Goussetis, “A highly integrated multipolarization wideband rectenna for simultaneous wireless information and power transfer (SWIPT),” *IEEE Trans. Antennas Propag.*, vol. 71, no. 10, pp. 7980–7991, Oct. 2023.
[12] M. Ali, G. Yang, and R. Dougal, “A new circularly polarized rectenna for wireless power transmission and data communication,” *IEEE Antennas Wireless Propag. Lett.*, vol. 4, pp. 205–208, 2005.
[13] X.-X. Yang, C. Jiang, A. Z. Elsherbeni, F. Yang, and Y.-Q. Wang, “A novel compact printed rectenna for data communication systems,” *IEEE Trans. Antennas Propag.*, vol. 61, no. 5, pp. 2532–2539, May 2013.
[14] M. Zada, I. A. Shah, J. Nasir, A. Basir, and H. Yoo, “Empowering remote patient monitoring with a dual-band implantable rectenna system for wireless power and data transfer,” *IEEE Trans. Antennas Propag.*, vol. 71, no. 12, pp. 9509–9522, Dec. 2023.
[15] P. Lu, X.-S. Yang, and B.-Z. Wang, “A two-channel frequency reconfigurable rectenna for microwave power transmission and data communication,” *IEEE Trans. Antennas Propag.*, vol. 65, no. 12, pp. 6976–6985, Dec. 2017.

[16] P. Lu, C. Song, and K. M. Huang, “A two-port multipolarization rectenna with orthogonal hybrid coupler for simultaneous wireless information and power transfer (SWIPT),” *IEEE Trans. Antennas Propag.*, vol. 68, no. 10, pp. 6893–6905, Oct. 2020.

[17] R. Dehbashi, K. Forooraghi, and Z. Atlasbaf, “Dual-fed antenna for wireless power transmission and data communication,” in *Proc. IEEE Antennas Propag. Soc. Int. Symp.*, Jul. 2006, pp. 2201–2204.

[18] S. Bi, Y. Zeng, and R. Zhang, “Wireless powered communication networks: An overview,” *IEEE Wireless Commun.*, vol. 23, no. 2, pp. 10–18, Apr. 2016.

[19] I. A. Hemadeh, K. Satyanarayana, M. El-Hajjar, and L. Hanzo, “Millimeter-wave communications: Physical channel models, design considerations, antenna constructions, and link-budget,” *IEEE Commun. Surveys Tuts.*, vol. 20, no. 2, pp. 870–913, 2nd Quart., 2018.

[20] B. Yang, Z. Yu, J. Lan, R. Zhang, J. Zhou, and W. Hong, “Digital beamforming-based massive MIMO transceiver for 5G millimeter-wave communications,” *IEEE Trans. Microw. Theory Techn.*, vol. 66, no. 7, pp. 3403–3418, Jul. 2018.

[21] G. Kou, X. Li, W. Zhao, K. Li, J. Zhang, and Z. Qi, “Low-cost broadband and high-gain millimeter-wave phased array based on high-order-mode back-cavity slot antenna,” *IEEE Trans. Antennas Propag.*, vol. 72, no. 11, pp. 8846–8851, Nov. 2024.

[22] J. Zhang and H. Wong, “A high-gain millimeter-wave Fabry–Perot cavity antenna with phase correction on a meta-ground reflective surface,” *IEEE Trans. Antennas Propag.*, vol. 72, no. 8, pp. 6187–6194, Aug. 2024.

[23] S. Wang, A. Alhamed, and G. M. Rebeiz, “An 8-element 5G multistandard 28-/39-GHz dual-band, dual-polarized phased array for compact systems,” *IEEE Trans. Microw. Theory Techn.*, vol. 71, no. 9, pp. 4109–4118, Sep. 2023.

[24] C. Song et al., “Highly efficient wideband mmWave rectennas for wireless power transfer system with low-cost multinode tracking capability,” *IEEE Trans. Antennas Propag.*, vol. 71, no. 11, pp. 8773–8787, Nov. 2023.

[25] B. Jiang, P. Li, S. Zheng, Y. Lin, and H. Xu, “A 24-GHz beam-steerable multinode wireless power transfer system with a maximum DC output of 5.7 dBm at 1-m distance,” *IEEE Trans. Microw. Theory Techn.*, vol. 72, no. 11, pp. 6774–6789, Nov. 2024.

[26] Y. Wang, H. Pan, and T.-T. Chan, “A dual-band dual-sense circularly polarized rectenna for millimeter-wave power transmission,” *IEEE Trans. Antennas Propag.*, vol. 73, no. 1, pp. 96–107, Jan. 2025.

[27] Y. Wang, X.-X. Yang, G.-N. Tan, and S. Gao, “Study on millimeter-wave SIW rectenna and arrays with high conversion efficiency,” *IEEE Trans. Antennas Propag.*, vol. 69, no. 9, pp. 5503–5511, Sep. 2021.

[28] M. Wagih, G. S. Hilton, A. S. Weddell, and S. Beeby, “Millimeter-wave power transmission for compact and large-area wearable IoT devices based on a higher order mode wearable antenna,” *IEEE Internet Things J.*, vol. 9, no. 7, pp. 5229–5239, Apr. 2022.

[29] Z. Yue et al., “Efficient and highly integrated millimeter-wave receiver for simultaneous wireless information and power transfer in sensor networks,” *IEEE Sensors J.*, vol. 25, no. 4, pp. 6534–6540, Feb. 2025.

[30] A. Mavaddat, S. H. M. Armaki, and A. R. Erfanian, “Millimeter-wave energy harvesting using 4 × 4 microstrip patch antenna array,” *IEEE Antennas Wireless Propag. Lett.*, vol. 14, pp. 515–518, 2015.

[31] M. Wagih, G. S. Hilton, A. S. Weddell, and S. Beeby, “Broadband millimeter-wave textile-based flexible rectenna for wearable energy harvesting,” *IEEE Trans. Microw. Theory Techn.*, vol. 68, no. 11, pp. 4960–4972, Nov. 2020.

[32] F. Deng and K. M. Luk, “A broadband high-gain multibeam ambient millimeter-wave energy-harvesting system,” *IEEE Internet Things J.*, vol. 11, no. 3, pp. 4888–4898, Feb. 2024.

[33] Y. Zhang, R. Huang, G. Wang, Z. H. Jiang, and W. Hong, “A low-cost polarization detection approach enabled by energy harvesting metasurface: Concept, design, and experiment,” *IEEE Trans. Microw. Theory Techn.*, vol. 72, no. 10, pp. 6174–6186, Oct. 2024.

[34] J. Sang, L. Qian, M. Li, J. Wang, and Z. Zhu, “A wideband and high-gain circularly polarized antenna array for radio-frequency energy harvesting applications,” *IEEE Trans. Antennas Propag.*, vol. 71, no. 6, pp. 4874–4887, Jun. 2023.

[35] H. Mei, X. Yang, B. Han, and G. Tan, “High-efficiency microstrip rectenna for microwave power transmission at Ka band with low cost,” *IET Microw., Antennas Propag.*, vol. 10, no. 15, pp. 1648–1655, Dec. 2016.

[36] S. Ladan, A. B. Guntupalli, and K. Wu, “A high-efficiency 24 GHz rectenna development towards millimeter-wave energy harvesting and wireless power transmission,” *IEEE Trans. Circuits Syst. I, Reg. Papers*, vol. 61, no. 12, pp. 3358–3366, Dec. 2014.

[37] W. Huang, J. Du, X.-X. Yang, W. Che, and S. Gao, “A novel 24 GHz circularly polarised metasurface rectenna,” *IET Microw., Antennas Propag.*, vol. 17, no. 6, pp. 419–426, May 2023.

[38] J. Shi et al., “A high-efficiency, simple-structure, compact wideband microwave energy harvester for wirelessly powered IoT receivers,” *IEEE Internet Things J.*, vol. 12, no. 13, pp. 23510–23523, Jul. 2025.

[39] K. Zhou, C.-X. Zhou, and W. Wu, “Resonance characteristics of substrate-integrated rectangular cavity and their applications to dual-band and wide-stopband bandpass filters design,” *IEEE Trans. Microw. Theory Techn.*, vol. 65, no. 5, pp. 1511–1524, May 2017.

[40] L. I. Parad and R. L. Moynihan, “Split-tee power divider,” *IEEE Trans. Microw. Theory Techn.*, vol. MTT-13, no. 1, pp. 91–95, Jan. 1965.

[41] D. M. Pozar, *Microwave Engineering: Theory and Techniques*. Hoboken, NJ, USA: Wiley, 2021.

[42] S.-P. Gao, W. Hu, H. Zhang, and Y. Guo, “Millimeter-wave rectifiers using proprietary Schottky diodes: Diode modeling and rectifier analysis,” in *Proc. Wireless Power Week (WPW)*, Jul. 2022, pp. 180–184.

[43] V. Marian, C. Vollaire, J. Verdier, and B. Allard, “Potentials of an adaptive rectenna circuit,” *IEEE Antennas Wireless Propag. Lett.*, vol. 10, pp. 1393–1396, 2011.

[44] C. A. Balanis, *Antenna Theory: Analysis and Design*. Hoboken, NJ, USA: Wiley, 2016.

Jiupei Shi received the B.S. degree in electronics science and technology and the M.S. degree in radio physics from Xinyang Normal University, Xinyang, China, in 2018 and 2022, respectively. She is currently pursuing the Ph.D. degree in information and communication engineering at Shenzhen University, Shenzhen, China.

Her research interests include mmWave antennas, RF energy harvesting, wireless power transmission, and simultaneous wireless information and power transfer.

Chaoyun Song (Senior Member, IEEE) received the B.E., M.S., and Ph.D. degrees in electrical engineering and electronics from the University of Liverpool, Liverpool, U.K., in 2012, 2013, and 2017, respectively.

He was an Assistant Professor with the School of Engineering and Physical Sciences, Heriot-Watt University, Edinburgh, Scotland, U.K. He is currently a Distinguished Professor with the State Key Laboratory of Radio Frequency Heterogeneous Integration, Shenzhen University, Shenzhen, China, and an Associate Professor (Senior Lecturer) with the Department of Engineering, King’s College London, London, U.K. He has published more than 150 articles (including 59 in IEEE TRANSACTIONS) in peer-reviewed journals and conference proceedings. His current research interests include wireless energy harvesting and power transfer, rectifying antennas (rectennas), flexible and stretchable electronics, metamaterials and metasurfaces, and low-power sensors.

Dr. Song was a recipient of numerous international awards, including the inaugural Best Paper Award of the *Proceedings of the IEEE*, the IEEE AP-S Young Professional Ambassador 2023, the IEEE AP-S Raj Mittra Travel Grant 2023, the EuCAP 2023 Best Antenna Paper Award, the IET Innovation Award in 2018, and the BAE Systems Chairman’s Award in 2017. Additionally, he has served as the Session Chair and/or TPC Member for various conferences, including EuCAP2018, IEEE AP-S Symposium 2021, IEEE VTC2022-fall, EuCAP2023, IEEE AP-S Symposium 2023, and EuCAP2024. He has consistently contributed as a reviewer for esteemed journals such as *Nature Electronics*, *Nature Communications*, *Advanced Materials*, *Advanced Functional Materials*, and *Nano Energy*, in addition to reviewing for over 15 IEEE TRANSACTIONS. He is a Top-200 reviewer of IEEE TRANSACTIONS ON ANTENNAS AND PROPAGATION (2021–2023). He has also taken on the role of guest editor for prestigious publications, including IEEE ANTENNAS AND WIRELESS PROPAGATION LETTERS, IEEE OPEN JOURNAL OF ANTENNAS AND PROPAGATION, and *IET Electronic Letters*.

Yejun He (Senior Member, IEEE) received the Ph.D. degree in information and communication engineering from the Huazhong University of Science and Technology, Wuhan, China, in 2005.

From 2005 to 2006, he was a Research Associate with the Department of Electronic and Information Engineering, The Hong Kong Polytechnic University, Hong Kong. From 2006 to 2007, he was a Research Associate with the Department of Electronic Engineering, Faculty of Engineering, The Chinese University of Hong Kong, Hong Kong. Since 2006, he has been a Faculty Member at Shenzhen University, Shenzhen, China, where he is currently a Full Professor with the College of Electronics and Information Engineering; the Director of the Sino-British Antennas and Propagation Joint Laboratory of Ministry of Science and Technology; the Director of Guangdong Engineering Research Center of Base Station Antennas and Propagation; and the Director of Shenzhen Key Laboratory of Antennas and Propagation. In 2012, he joined the Department of Electrical and Computer Engineering, University of Waterloo, Waterloo, ON, Canada, as a Visiting Professor. From 2013 to 2015, he was an Advanced Visiting Scholar (a Visiting Professor) with the School of Electrical and Computer Engineering, Georgia Institute of Technology, Atlanta, GA, USA. From 2023 to 2024, he was an Advanced Research Scholar (a Visiting Professor) with the Department of Electrical and Computer Engineering, National University of Singapore, Singapore. He was selected as an Expert with Special Government Allowance from the State Council in China and a Leading Talent in “Guangdong Special Support Program” in 2024. He was promoted to Shenzhen “Pengcheng Scholar” Distinguished Professor in 2020. He is the principal investigator for more than 40 current or finished research projects, including the National Natural Science Foundation of China, the Science and Technology Program of Guangdong Province, and the Science and Technology Program of Shenzhen City. He has authored or co-authored more than 360 refereed journal articles and conference papers, and seven books. He holds more than 30 patents. His research interests include wireless communications, antennas, and radio frequency.

Dr. He is a Fellow of IET and a Fellow of China Institute of Communications. He was a Technical Program Committee Member or the Session Chair for various conferences, including the IEEE Global Telecommunications Conference, the IEEE International Conference on Communications, the IEEE Wireless Communication Networking Conference, and the IEEE Vehicular Technology Conference. He was selected as a Board Member of the IEEE Wireless and Optical Communications Conference. He was a recipient of Shenzhen Overseas High-Caliber Personnel Level B (Peacock Plan Award B), Shenzhen High-Level Professional Talent (Local Leading Talent), the Second Prize of Shenzhen Science and Technology Progress Award in 2017, the Three Prize of Guangdong Provincial Science and Technology Progress Award in 2018, the Second Prize of Guangdong Provincial Science and Technology Progress Award in 2023, and the 10th Guangdong Provincial Patent Excellence Award in 2023. He was a reviewer of various journals, such as IEEE TRANSACTIONS ON VEHICULAR TECHNOLOGY, IEEE TRANSACTIONS ON COMMUNICATIONS, IEEE TRANSACTIONS ON INDUSTRIAL ELECTRONICS, IEEE TRANSACTIONS ON ANTENNAS AND PROPAGATION, IEEE WIRELESS COMMUNICATIONS, IEEE COMMUNICATIONS LETTERS, *International Journal of Communication Systems, and Wireless Personal Communications*. He is the Chair of the IEEE Antennas and Propagation Society-Shenzhen Chapter and obtained the 2022 IEEE APS Outstanding Chapter Award. He was the TPC Chair of IEEE ComComAp 2021 and the General Chair of IEEE ComComAp 2019. He was the TPC Co-Chair of WOCC 2023/2022/2019/2015, APCAP 2023, UCMMT 2023, ACES-China2023, and NEMO 2020. He was the Publicity Chair of several international conferences, such as the IEEE PIMRC 2012. He was the Executive Chair of the 2024/2025 IEEE International Workshop of Radio Frequency and Antenna Technologies and is acting as the Executive Chair of the 2026 IEEE International Conference of Radio Frequency and Antenna Technologies. He is an Associate Editor of IEEE TRANSACTIONS ON VEHICULAR TECHNOLOGY, IEEE TRANSACTIONS ON ANTENNAS AND PROPAGATION, IEEE TRANSACTIONS ON MOBILE COMPUTING, IEEE ANTENNAS AND WIRELESS PROPAGATION LETTERS, IEEE ANTENNAS AND PROPAGATION MAGAZINE, *International Journal of Communication Systems*, *China Communications*, and *ZTE Communications*.

Qiang Hua (Member, IEEE) received the B.Sc. degree in communication engineering from the University of Liverpool, Liverpool, U.K., in 2016, the M.Sc. degree in digital signal processing from The University of Manchester, Manchester, U.K., in 2017, and the Ph.D. degree from the University of Liverpool, in 2022, entitled “Advanced Antenna Designs for 5G Communications.”

In 2021, he was a Research Assistant at the Built Environment and Sustainable Technologies (BEST) Research Institute, where he developed novel sensor designs to detect insecticides on walls and worms in human blood. In 2023, he became a Lecturer at the School of Computing and Engineering at the University of Huddersfield, Huddersfield, U.K., where he is a Senior Lecturer in electrical engineering at the School of Computing and Engineering. His current research interests include the base station antenna design for 5G in wireless communications, new material antennas, smart sensors for health monitoring, wearable devices, and machine learning methods for antenna optimization.

Dr Hua is a Fellow of the Higher Education Academy (FHEA) and a member of the IET.

Bo Liu (Senior Member, IEEE) received the B.Eng. degree from Tsinghua University, Beijing, China, in 2008, and the Ph.D. degree from the University of Leuven (KU Leuven), Leuven, Belgium, in 2012.

From 2012 to 2013, he was a Humboldt Research Fellow and was working with the Technical University of Dortmund, Dortmund, Germany. In 2013, he was appointed a Lecturer (Assistant Professor) at Wrexham Glyndwr University, U.K., where he was promoted to a Reader in 2016. He is a Professor of electronic design automation at the University of Glasgow, Glasgow, U.K. He has authored or co-authored one book and more than 100 articles in renowned international journals, edited books, and conference proceedings. His research interests lie in AI-driven design methodologies of microwave devices, analog/RF integrated circuits, evolutionary computation, and machine learning. In terms of AI-driven antenna design, he is the inventor of the SADEA algorithm series.

Junjie Zheng (Graduate Student Member, IEEE) was born in Guangdong, China, in 2000. He received the B.Eng. degree from Guangdong University of Petrochemical Technology, Maoming, China, in 2022. He is currently pursuing the M.S. degree in electronic science and technology at Shenzhen University, Shenzhen, China.

His research interests encompass wireless power transfer systems, flexible sensor integration technologies, and metamaterial-based antenna design, with a current focus on innovative applications of metasurfaces in energy transmission and sensing platforms.

Jinyao Zhang received the B.Eng. degree in electrical and electronic engineering from the University of Liverpool, Liverpool, U.K., in 2018, and the Ph.D. degree from the University of Liverpool in 2023.

In 2024, he joined the School of Electronic and Information Engineering, Shenzhen University, Shenzhen, China, as a Post-Doctoral Researcher. His research focuses on wireless power transfer, microwave energy harvesting, simultaneous wireless information and power transfer, metasurface antenna, and rectenna design.

Sai-Wai Wong (Senior Member, IEEE) received the B.S. degree in electronic engineering from The Hong Kong University of Science and Technology, Hong Kong, in 2003, and the M.Sc. and Ph.D. degrees in communication engineering from Nanyang Technological University, Singapore, in 2006 and 2009, respectively.

From July 2003 to July 2005, he was an Electronics Engineer to lead the Electronic Engineering Department in China with two Hong Kong manufacturing companies. From May 2009 to October 2010, he was a Research Fellow with the ASTAR Institute for Infocomm Research, Singapore. Since 2010, he has been an Associate Professor and later became a Full Professor at the School of Electronic and Information Engineering, South China University of Technology, Guangzhou, China. Since 2017, he has been a tenured Full Professor with the College of Electronics and Information Engineering, Shenzhen University, Shenzhen, China. His current research interests include RF/microwave circuit and antenna design and integrated sensing and communication (ISAC).

Dr. Wong was a recipient of the New Century Excellent Talents in University, awarded by the Ministry of Education of China in 2013, and Shenzhen Overseas High-Caliber Personnel Level C in 2018.

Yi Huang (Fellow, IEEE) received the B.Sc. degree in physics from Wuhan University, Wuhan, China, in 1984, the M.Sc. (Eng.) degree in microwave engineering from NRIET, Nanjing, China, in 1987, and the D.Phil. degree in communications from the University of Oxford, Oxford, U.K., in 1994.

In 1994, he was a Research Fellow at British Telecom Laboratories before joining the Department of Electrical Engineering and Electronics, University of Liverpool, Liverpool, U.K., in 1995, where he is currently a Full Professor of wireless engineering and the Head of the High-Frequency Engineering Group. Since 1987, he has been actively engaged in research on antennas, wireless communications, radar, EMC, and applied electromagnetics. More recently, his focus has expanded to include novel materials for antennas, wireless energy harvesting, and power transfer. His professional experience includes three years as a Radar Engineer at NRIET and research positions at the University of Birmingham, Birmingham, U.K.; University of Oxford, Oxford, U.K.; and University of Essex, Colchester, U.K. He has published more than 500 peer-reviewed articles in leading international journals and conferences. He is the author of several books, including *Antennas: From Theory to Practice* (Wiley, 2008 and 2021) and *Reverberation Chambers* (Wiley, 2016 and 2019).

Dr. Huang is a Senior Fellow of the Higher Education Academy (SFHEA), a College Member of EPSRC, and a Member of the IEEE AP-S New Technology Directions Committee. His contributions have earned him more than ten prestigious awards, such as the IET Premium Award 2022 for Best Paper, the EuCAP 2023 Best Antenna Paper, the IET Innovation Award 2018, and the BAE Systems Chairman's Award 2017. He has secured numerous research grants from research councils, government agencies, charities, EU, and industry, and has acted as a consultant to various companies. He has served on multiple national and international technical committees, including the IET, EPSRC, European ACE, COST-IC0603, COST-IC1102, and EurAAP. He has also held editorial roles for leading journals, serving as an Associate Editor and Guest Editor for four international journals, including IEEE AWPL (2016–2022), and the Editor-in-Chief of *Wireless Engineering and Technology* from 2014 to 2023. He was U.K./Ireland Delegate to EurAAP (2016–2020) and has been a keynote/invited speaker and organizer of numerous international conferences and workshops, such as EuCAP, IEEE iWAT, WiCom, and LAPC. He is an Associate Editor of IEEE TRANSACTIONS ON ANTENNAS AND PROPAGATION. He is a Distinguished Lecturer of IEEE AP-S. More information can be found at https://www.liverpool.ac.U.K./people/yi-huang